7.5 DERIVATION OF TRUE STRESS-TRUE STRAIN CONSTITUTIVE LAWS FOR IRRADIATED FERRITIC STEELS -T. Yamamoto, G. R. Odette, S. Li (University of California Santa Barbara), S. Maloy, T. Saleh (Los Alamos National Laboratory)

OBJECTIVE

The objective of this study is to derive true stress-stain constitutive [σ(ε)] laws for irradiated candidate fusion reactor structural materials.

SUMMARY

In previous studies we developed a self-consistent approach to derive true stress-stain constitutive [σ(ε)] laws for 8Cr-2W tempered martensitic steel, F82H, encompassing a range of unirradiated and irradiated conditions [1]. In this report, five 8-12Cr tempered martensitic steels and one 14Cr oxide dispersion strengthened alloy, that were side-by-side irradiated to 6.5 dpa at 295°C in the Advanced Test Reactor (ATR), were analyzed. The approach is based on simultaneous measurements and finite element method (FEM) simulations of engineering stress-strain s(e) curves, that are consistent with a unique σ(ε) law. In the irradiated condition, the σ(ε) fall into categories of: strain softening, nearly perfectly plastic and strain hardening. Increases in the average σ(ε) in the range of 0-10% strain are smaller than the corresponding increases in the yield stress and vary more from alloy to alloy.

PROGRESS AND STATUS

Introduction

Deformation controlled failure of a structure is mediated by the interaction of a number of intrinsic properties, including constitutive properties and plasticity laws, as well as extrinsic factors, such as geometry and loading conditions. Standard tensile tests directly provide data for engineering stress and strain, s(e), defined in the usual way: s given by load divided by the initial cross section area and e by the change in gauge length divided by its original length. Tensile properties are usually simply characterized by the engineering yield stress $s_y \approx \sigma_y$, the ultimate stress (s_{uts}), the uniform elongation (e_u) at the onset of necking, the total elongation (e_t) and the reduction in area (RA), both at specimen rupture. Note, the so-called ductility and post yield stress measures are not true material properties, since they depend on the deformed body cross-section shape and dimensions. It is trivial to convert s(e) to σ ε) up to the point of necking using the relation of $\sigma(\varepsilon) = s(e)(1+e)$ and $\varepsilon = \ln(1+e)$. However, due to typically very low e_u after irradiation, tensile test s(e) that undergo nearly immediate necking cannot directly provide post-yielding σ(ε). Plastic strains increase rapidly to high values in the necked region undergoing large geometry changes (LGC), where continued deformation occurs under complex tri-axial stress states. The σ(ε) derived from tensile tests are assumed to represent effective stress and strain that can be used under arbitrary multi-axial loading conditions. Modeling plastic deformation also requires a proper description of the governing flow potential (like J_2 flow theory) and associated flow-hardening rules. As described below, s(e) curves can be used to derive σ(ε) up to large ε by iterative FEM calculations. The FEM meshing is shown in Figure 1.

Approach

The post yield total flow stress can be decomposed into the yield stress and a strain hardening component as:

$$\sigma(\varepsilon,\dot{\varepsilon},T) = \sigma_y(\dot{\varepsilon},T) + \sigma_{pl}(\varepsilon,\dot{\varepsilon},T) \tag{1}$$

Or more simply for a given $\dot{\varepsilon}$ and T:

$$\sigma(\varepsilon) = \sigma_y + \sigma_{pl}(\varepsilon) \tag{2}$$

Experimental s(e) data was directly converted to $\sigma(\varepsilon)$ up to the necking instability strain (or uniform elongation), ε_u. The strain hardening $d\sigma/d\varepsilon$ (= $d\sigma_{pl}/d\varepsilon$) derived from the $\sigma(\varepsilon)$ at $\varepsilon \leq \varepsilon_u$ was fitted to modified Voce-Mecking model [2], that describes the change in dislocation density (ρ) as the competition of dislocation storage with increasing strain and annihilation rates controlled by ρ. The model can be rewritten in terms of the strain hardening, σ_{pl}, using the dislocation to hardening relation, $\sigma_{pl} = M\alpha\mu b\sqrt{\rho}$, where M is Taylor factor, α is the strength factor, μ is shear modulus and b is Burgers vector as:

$$d\sigma_{pl}/d\varepsilon = P_1/\sigma_{pl} - P_2\sigma_{pl} = P_1/(\sigma_t - \sigma_o) - P_2(\sigma_t - \sigma_o) \qquad (3)$$

Integration of Eq. 3 with a boundary condition of $\sigma(\varepsilon_o) = \sigma_o$ gives the following function form that saturates at $\sigma_{pl,sat} = (P_1/P_2)^{1/2}$ or $\sigma_{t,sat} = \sigma_o + (P_1/P_2)^{1/2}$.

$$\sigma_{pl} = \sqrt{\frac{P_1 - \left(P_1 - P_2\sigma_o^2\right)\exp(-2P_2(\varepsilon_p - \varepsilon_o)}{P_2}}\ ) \qquad (4)$$

The fitted P_1, P_2, and σ_o were used to extrapolate $\sigma(\varepsilon)$ up to a steady state saturation at $d\sigma/d\varepsilon = 0$. The fitted model was used to perform the finite element (FE) simulations of the tests using the ABAQUS 6.11.2 software package with a three-dimensional mesh, consisting of ≈ 1400 brick elements that, as shown in Figure 1, models 1/8 of a tensile specimen gauge section. In most cases the initial $\sigma(\varepsilon)$ model that fits best to the experimental data up to the necking does not work to simulate post-necking behavior. So the input $\sigma(\varepsilon)$ was iteratively adjusted until the FE engineering s(e) prediction matched the experimental curve. A proper $\sigma_{s,sat}$ often worked in unirradiated condition. However, in many cases for the irradiated condition it did not. In these cases the simulated s(e) is persistently higher than experimental value, even taking σ_{sat} as low as ≈ $\sigma(\varepsilon_u)$ at the point of necking. This signals that strain softening needs to be considered.

Assuming that softening occurs due to defect free bands formed as a result of moving dislocations interacting with irradiation induced defects, which presumably are dislocation loops, a part of the irradiation induced increase of yield stress is recovered as a function of plastic strain, ε_{pl} as:

$$\sigma_y = \sigma_y - \sigma_{ssat}\left\{1 - \exp\left(-K\varepsilon_{pl}\right)\right\} \qquad (5)$$

Here $\sigma_{s,sat}$ and K are both fitting parameters for the maximum and rate constant of softening, respectively. Figure 2 shows an example of fitted $\sigma_y(\varepsilon)$ function along with total $\sigma(\varepsilon)$ and $\sigma_{pl}(\varepsilon)$. Two competing effects of hardening in $\sigma_{pl}(\varepsilon)$ and softening in $\sigma_y(\varepsilon)$ create peaking $\sigma(\varepsilon)$ right after the necking.

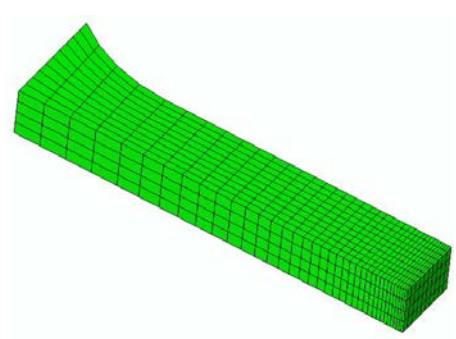

Figure 1. An example of 3D model used in a finite element method simulation of tensile tests.

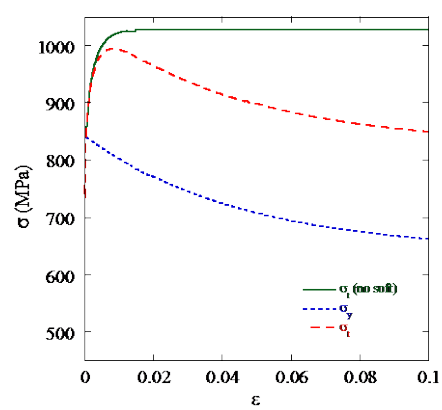

Figure 2. An example of hardening-softening constitutive models.

Our method to deriving $\sigma(\varepsilon)$ also includes quantifying large geometry changes (LGC) and deformation-flow (micro to macro) patterns of strain distribution (SD) for a wide variety of test geometries. This allows access to high stains and provides additional constraints on $\sigma(\varepsilon)$. For tensile specimens LGC is characterized by the evolution of the necked region geometry. Measured necking geometries were compared with corresponding simulations in FEM models in order to confirm the consistency of the $\sigma(\varepsilon)$.

Experimental details

The post-irradiation examination results reported here are from a large, multipurpose University of California Santa Barbara led irradiation program carried out in the Advanced Test Reactor (ATR) at the Idaho National Laboratory (INL), as part of the ATR Nuclear Science Users Facility (NSUF) Program [3]. One of many purposes of the UCSB ATR-1 experiment was to irradiate a large number of candidate structural alloys "side by side", at nearly identical temperatures and dpa, so that relatively direct comparisons of changes in their microstructures (not discussed here) and mechanical properties could be made, without many of the usual confounding factors encountered in analyzing results from different irradiations. Here we focus on five 8-12Cr TMS and one ODS alloy. The TMS include: HT-9 (H9), T91, F82H-IAEA (F2), NF616 (N6) and Eurofer97 (E9), where the (X#) notation indicates the compact alloy identification code used here. The measured alloy compositions and the TMS normalized and tempered heat treatments are summarized in Table 1. This MA957 ODS alloy was processed by ball milling Y_2O_3 and elemental powders, followed by consolidation via hot extrusion at ≈ 1100°C [4].

The irradiation was carried out in the A10 position in the ATR over a range of nominal temperatures from ≈ 290 to 750°C, and displacement damage doses from ≈ 1.7 to 6.5 dpa. A large number and wide range of specimen types (1375 in total) were contained in 32 UCSB designed sub-packets that optimized gas gap temperature control and minimized the corresponding specimen temperature uncertainties in the un-instrumented drop-in the ATR A10 position test train. The as-run fluxes and fluences were calculated by the MCNP code, and varied over the 110 cm length of the 10 mm ID capsule, with a mid-core peak of flux ≈ 2.3×10^{14} n/cm^2-s (E > 1 MeV), corresponding to ≈ 3.5×10^{-7} dpa/s, and a fluence ≈ 4×10^{21} n/cm^2/s. The temperatures were determined by detailed finite element thermal analyses conducted independently by both UCSB and INL. Further details on the UCSB ATR-1 experiment are described elsewhere [3]. The average irradiation conditions for the tensile specimens were ≈ 296°C and 6.5 dpa.

The tensile tests were carried out in the LANL CMR hot cells, on an Instron 5567 screw driven test machine, at a strain rate of 5×10^{-4}/s at both ≈ 25°C and 300°C, using sub-size SSJ2 type specimens with gauge dimensions of 5 mm length, 1.2 mm width and 0.5 mm thickness. The specimens were shoulder loaded to provide good alignment in tension. The elevated temperature tensile tests were performed in an inert argon atmosphere. In general, two irradiated tests were carried out at 25°C, but only one test was conducted at 300°C. The redundant s(e) curves at 25°C were very similar in all cases. The raw digitized load and load point displacement data were converted to nominal engineering stress-strain s(e) curves, that were subsequently used for the derivation of the $\sigma(\varepsilon)$.

Table 1. Alloy Composition (wt.%) and Heat Treatments

Alloy	C	Cr	Mn	Ni	Si	Mo	Nb	V	W	O	N	P	Y_2O_3	Al/Cu/Co/Ti	Fe
HT-9	.201	12.49	.41	.60	.28	1.07	<.002	.29	.52	.002	.001	.007	<.0005	.015	Bal
Eurofer97	.117	8.69	.47	.024	.056	.005	<.002	.20	.82	.003	.023	.004	.002	.009	Bal
F82H	.093	7.89	.16	.026	.12	.005	<.002	.16	1.21	.003	.008	.004	.002	.002	Bal
NF616	.108	9.71	.46	.064	.056	.47	.043	.20	1.22	.003	.060	.007	.001	.003	Bal
T91	.052	9.22	.46	.18	.24	.96	.063	.24	.013	.002	.057	.016	.001	.009	Bal
MA 957	0.02	13.57	0.07	0.10	0.03	0.30	<0.002	--	--	0.22	---	0.004	0.25	1.1	Bal

Heat Treatments: HT9- 1040°C-1hr./air cool, 760°C 1hr./air cool; T91- 1040°C-1hr./air cool, 760°C 1hr./air cool; F82H IAEA- 1040°C-40min./air cool, 750°C 1hr./air cool; Eurofer97- 980°C-27min./air cool, 760°C 90min./air cool; NF616- Hot Rolled at 1025°C/air cool; 750°C-2hr./air cool

Results and Discussion

The iterative FE method described above was used to extract true stress-true strain constitutive laws, $\sigma(\varepsilon)$, from engineering s(e) curves. Figure 3 shows the results for both unirradiated and irradiated conditions on

a consistent e or ε-scale up to 50%. Figures 3a - l summarize the results of the analysis for the six alloys in this study at 25°C (3a-f) and 300°C (3g-l), respectively. Each plot for a specific alloy shows the unirradiated (blue) and irradiated (red) s(e) curves (heavy dashed lines) along with the corresponding derived σ(ε) curves (heavy dotted lines) and the converged FEM prediction of the s(e) curve (light solid line). Figure 4 shows limited comparisons of FEM predicted reduction of area (RA) at an onset for fracture, while Figure 5 shows a few examples of shape comparisons. More specifically FEM geometry was evaluated at the corresponding strain that a rapid drop in experimental s(e) is observed. This may cause some differences that are associated with early damage development that ultimately leads to fracture. In the future more direct comparisons will include continuous monitoring of the LGC in the neck and strain-mapping by digital image correlation. As shown by the red regions in the FEM cross sectional images in Figure 5, the center of the neck thins more than at the corners of the rectangular simulation section. The LGC pattern is also observed experimentally. The average of the center and corner thicknesses was used to calculate these RA, and compared to experiment when both thicknesses measurements were available. However in some tests only a side view was measured to evaluate corner thickness. The shrinkage at the corner is often more pronounced in the experiments than in the FEM simulations, probably due to the assumption of ideally sharp starting corners, while in reality they have a finite radius that enhances the actual thickness reduction. Better approaches to LGC evaluation will also be pursued in the future work. Nevertheless, the LGC comparisons between the FEM models and experimental observations are very encouraging. In most cases differences are only a few percent; larger differences are associated with limited LGC measurements. Hence, the LGC results provide a first order validation of the FEM simulation.

The derived σ(ε) have some common classes of behavior. The unirradiated alloys continuously strain harden, albeit at various rates. However, following irradiation the σ(ε) fall into one of three general categories:

- i) Strain softening up to $\varepsilon \approx$ 10-20%, followed by an approximately saturated constant, perfectly plastic σ(ε).
- ii) A small increment of strain hardening, followed by an approximately saturated constant, perfectly plastic σ(ε).
- Iii) Continuous strain hardening.

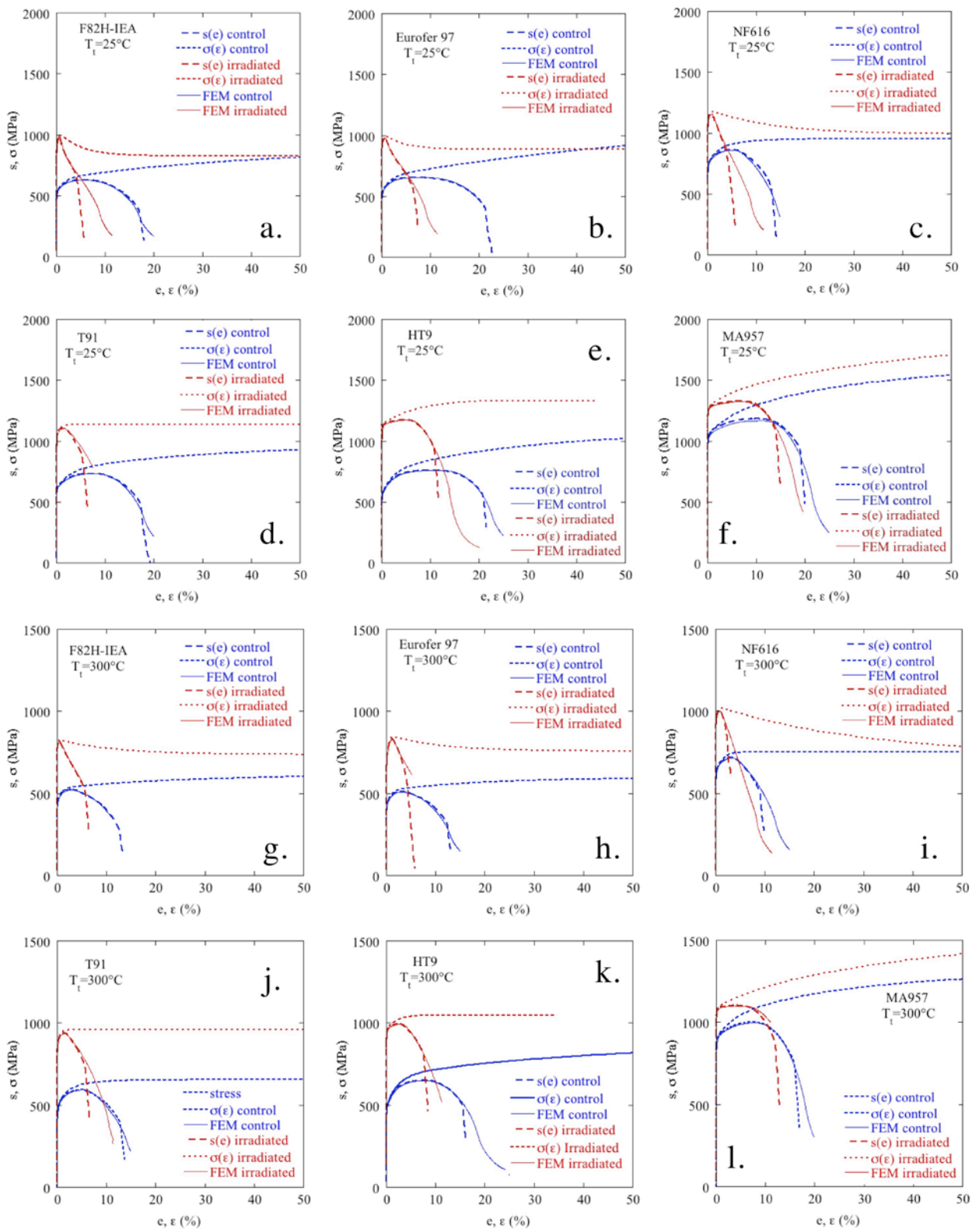

Figure 3. Experimental vs simulated s(e) curves along with derived σ(ε)□models for irradiated and unirradiated materials tested at 25°C (a-f) and 300°C (g-l).

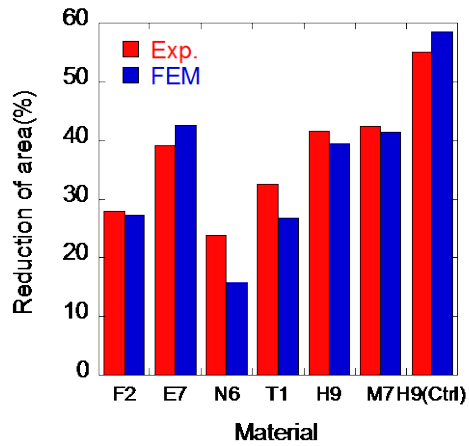

Figure 4. Comparison of the reduction of area at the fracture onset in FEM with that of fractured specimens in the tests.

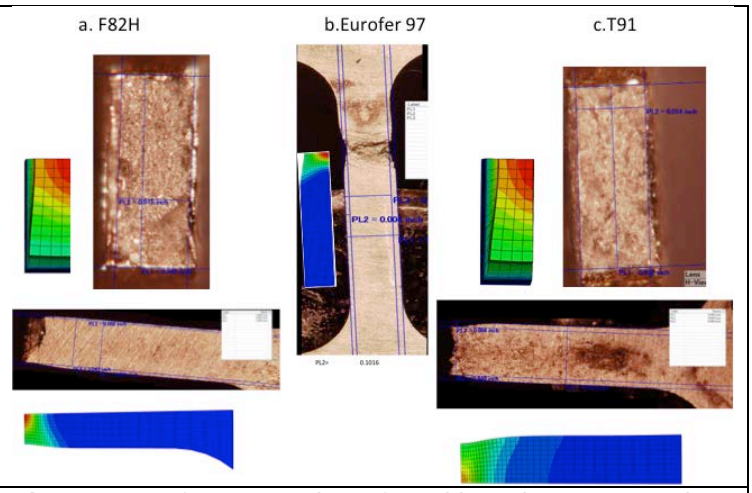

Figure 5. A few examples of necking shape comparison between FEM and experiments.

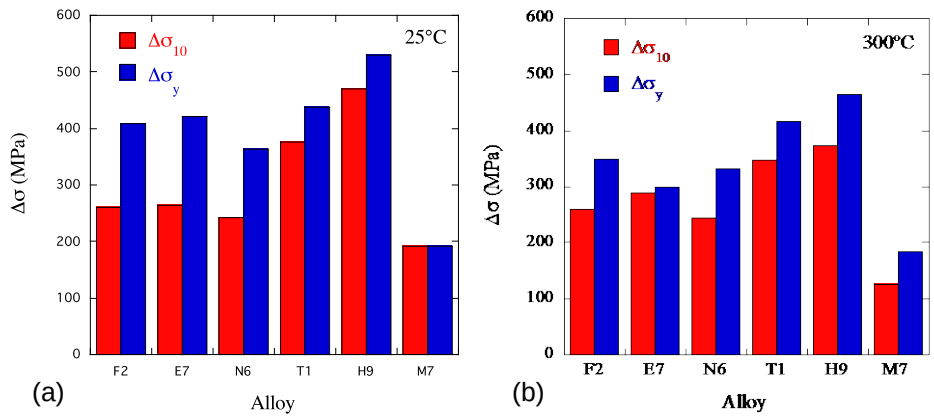

Figure 6. Changes in the average flow stress between 0 and 10% strain ($_{10}$) and the corresponding $_y$ for tests at: a) 25°C; b) 300°C.

For irradiated condition tests at 25°C, type i behavior is observed for F2, E9 and N6, type ii for T1 and type iii for H9 and M7. At 300°C the pattern is similar, but N6 continues to slowly soften up to 50% and the H9 displays type ii behavior. For tests at 25°C the FH, E7 and N6 irradiated $\sigma(\varepsilon)_i$ approach the unirradiated $\sigma(\varepsilon)_u$ at $\varepsilon \approx 50\%$, while the $\sigma(\varepsilon)_i$ remains higher for T1, H9 and M7. In the case of the 300°C tests, the $\sigma(\varepsilon)_i$ remain significantly higher than the $\sigma(\varepsilon)_u$ over the entire strain range examined. Note that we have previously carried out a similar analysis of F2 tensile test data from High Flux Isotope Reactor irradiations [1,5]. In the dose range of ≈ 4.9 to 18 dpa at ≈ 300°C and for strains up to 50%, one case showed strain softening, while another was closer to perfectly plastic with slight strain hardening following a nearly perfectly plastic low strain increment with slight softening. However, in a third case, significant, continuous strain hardening was observed after a small increment of perfectly plastic flow. And in all three cases at more than 7 dpa, strain hardening was found at even higher strains. Possible effects of high levels of He, produced in a spallation proton irradiation on $\sigma(\varepsilon)_i$ were also observed. The reasons for the similarities and differences between these previous and current results will be explored in future research.

As noted previously, the plastic strain range between 0 and 10% is especially important since this probably represents a practical structural limit and since this plastic strain range plays a dominant role in both hardness and fracture toughness [6,7]. Figure 6a and b compare the σ_y and the average flow stress between 0 and 10% ε ($\Delta\sigma_{10}$) for all the alloys at both 25 and 300°C, respectively. In general the changes in $\Delta\sigma_{10}$ are less than $\Delta\sigma_y$, with the largest differences for F2, E7 and N6 at 25°C. On average, $\Delta\sigma_{10} \approx 0.78\ \Delta\sigma_y$ at both test temperatures.

Conclusions

The true stress-true strain σ(ε) laws of five 8-12Cr tempered martensitic steels and one 14Cr oxide dispersion strengthened alloy, that were side-by side irradiated to 6.5 dpa at 295°C in the Advanced Test Reactor (ATR), were derived from tensile test results at 25 and 300°C, using iterative FE simulations of engineering s(e) curves.

The main results and conclusions include:

- For the irradiated alloys, the derived σ(ε) curves fall into categories of: strain softening, nearly perfectly plastic and strain hardening.
- Large geometry changes in necking behavior are also consistent between FEM simulation and experimental observation, while further study on more detailed shapes are planned in the future studies.
  Differences in the average σ(ε) increases in the range of 0-10% strain are smaller than the corresponding $\Delta\sigma_y$, and vary more from alloy to alloy. This has important implications to irradiated properties like fracture toughness.

Future Work

In addition to a wide range of applications of the σ(ε) laws derivation method, future research will be directed at understanding the differences in constitutive laws between the materials as well as the effects of irradiation.

Acknowledgements

The work at UCSB was funded by a DOE NEUP (NU-11-3150) and Office of Fusion Energy Science (DE-FG03-94ER54275) grants. The work at LANL was funded under the Advanced Fuels Campaign of the Department of Energy (DOE) Fuel Cycle Research and Development Program. The UCSB ATR-1 irradiations were carried out as part of the National Scientific Users Facility program, with the assistance of a large number of outstanding engineers. The help of Colin Knight in arranging shipment of the specimens from INL to LANL is greatly appreciated. Special thanks also go to UCSB staff members Doug Klingensmith and David Gragg who played the key roles in building the experiment and former PhD student, Dr. Nicholas Cunningham, who carried out the thermal design analysis.

References

[1] T. Yamamoto, G.R. Odette, Y. Wu, Fusion Materials Semi-annual Progress Report for Period Ending December 31, 2011, DOE/ER-0311/51, US Department of Energy, 78.
[2] P. Spatig, G. R. Odette, G. E. Lucas, M. Victoria, J. Nucl. Mater. 307-311 (2002) 536.
[3] G.R. Odette, T. Yamamoto, B. Sams, D. Klingensmith, N. Cunningham, G. Waches, J.I. Cole, P.E. Murrey, “Summary of the USCB Advanced Test Reactor National Scientific Users Facility Irradiation Experiment,” DOE/ER-0313/46 (2009) 79.
[4] G.R. Odette, M.J. Alinger, B.D. Wirth, Recent developments in irradiation-resistant steels, Annual Review of Materials Research, Annual Reviews, Palo Alto, 2008, pp. 471-503.
[5] T. Yamamoto, G.R. Odette, M.A. Sokolov, Journal of Nuclear Materials, 417 (2011) 115-119.
[6] G.R. Odette, M.Y. He, T. Yamamoto, Journal of Nuclear Materials, 367 (2007) 561-567.
[7] M.Y. He, G.R. Odette, T. Yamamoto, D. Klingensmith, J. Nucl. Mater. 367 (2007) 556-560.